Available online at www.sciencedirect.com

SciVerse ScienceDirect

Journal of the Franklin Institute 349 (2012) 2294–2312

Journal of The Franklin Institute

www.elsevier.com/locate/jfranklin

Effect of geometry on the performance of MEMS aluminum nitride trampoline resonators in longitudinal resonance

Annie Ruimi[a,*], Yueming Liang[b], Robert M. McMeeking[c,d]

[a]*Texas A&M University at Qatar, Department of Mechanical Engineering, Doha, Qatar*
[b]*Exxon Mobil, Houston, TX, USA*
[c]*University of California at Santa Barbara, Department of Mechanical Engineering, CA, USA*
[d]*University of California at Santa Barbara, Materials Department, CA, USA*

Received 10 June 2010; received in revised form 25 August 2011; accepted 5 September 2011
Available online 19 September 2011

Abstract

The performance of a microscale aluminum nitride piezoelectric resonator in the shape of a trampoline is analyzed using three-dimensional finite element simulations. The air-suspended resonator is supported by beams and is designed to respond to longitudinal through-thickness vibrations. The device is targeted to operate at UHF frequencies (3 GHz) suitable for wireless filtering applications. Energy loss due to material damping is accounted for in the model. Other sources of damping are considered. We analyze if and how the material thickness, number of beams and beam length affect the resonator performance. This is intended to provide useful information at the design stages and eliminate the high costs associated with manufacturing a filter with poor performance. Performance is evaluated by means of the electromechanical coupling coefficient (K^2) and the quality factor (Q) calculated from the electrical impedance frequency response plots. The results indicate that (i) K^2 is insensitive to geometry (K^2~6.5%), (ii) Q increases linearly with the AlN thickness attaining Q~1900 for a 1.7 μm thick resonator and (iii) a trampoline resonator with three beams has a better performance capability than the resonator with four or eight beams with a figure of merit K^2Q~120 and resonating at a higher frequency value than its counterparts resonators, peaking at 3.21 GHz. The performance figures agree well with those predicted by a one dimensional theory. The value of K^2 also agrees well with test data but that of Q is higher than the one recorded in the lab.

*Corresponding author.
E-mail addresses: annie.ruimi@qatar.tamu.edu (A. Ruimi), yueming_liang@yahoo.com (Y. Liang), rmcm@engineering.ucsb.edu (R.M. McMeeking).

0016-0032/$32.00
doi:10.1016/j.jfranklin.2011.09.005

1. Introduction

In the last ten years, there have been multiple research efforts to incorporate innovative microfabrication and material processing techniques to enhance the performance of ultra-high-frequency (UHF) filters such as those used in wireless communication devices [1–21]. Filters can be modeled as an arrangement of resonators of various levels of geometric complexity. Desirable features characteristic of a high performance filter include a small size, light weight, low production cost, a clear signal reception and minimum power consumption so filters of microscale dimensions provide an immediate solution to the size/weight reduction. In addition, microelectromechanical systems (MEMS)-based filters utilize technologies borrowed from the semiconductor industry and can be mass produced, which in turn reduces the manufacturing costs. As a result, functioning MEMS-filter components have been built but testing their performance in laboratory has been proven to be difficult and costly. On the other hand, an analytical analysis is not an option because piezoelectric problems have no-close form solutions except for very simple unrealistic geometric conditions so numerical simulations have become increasingly attractive tools to the MEMS community.

Both the transverse and longitudinal resonant frequency of a mechanical resonator depends on its material, geometry and mode of vibration [22]. The transverse resonant frequency varies as $(\pi/L)^2\sqrt{(EI/\rho A)}$ where L and A are the length and cross section area of the beam and where E and I are the modulus of elasticity and area moment of inertia. This relation shows that attaining frequencies in the UHF regime would require the difficult task to built resonators a few microns long. On the opposite, longitudinal resonant frequency varies as $f=NV_p/2h$ where N is the resonance order, h is the thickness of the oscillator and v_p is the material's acoustic velocity so resonators a few microns thick are capable of reaching frequencies in the UHF regime.

In this spirit, a multi-disciplinary team at the University of California at Santa Barbara (UCSB) has engaged in a research program aimed at developing a high performance through-thickness longitudinally vibrating resonator. Program tasks include design, fabrication and experimental as well as numerical characterization of the device. This paper reports on the numerical results. Whenever possible, we compare the results with test data obtained from the device fabricated at UCSB. The structure adopted by the team is a FBAR (Film Bulk Acoustic Resonator) using a piezoelectric film to provide an electrical input. It is clear from the relations above that the resonator geometry will affect the resonant frequency so the focus of the study is on determining how – rather than if – geometry will impact the performance.

Among the various FBAR structures described by Rosenbaum in his book on acoustic resonators [23], suspended plates have been reported as having the best potential for high performance. This provided the basis for the design of the device fabricated at UCSB [24] and shown in Fig. 1. It consists of nine circular resonators 300 μm in diameter, about 2 μm thick, suspended over a circular air-cavity. Eight beams at 45° apart each, 24 μm wide and 300 μm long connect the circular membrane to a surrounding silicon substrate. Because of their distinctive shape, we named the resonators "trampoline" resonators. The span between the resonators' centers is 1000 μm. The resonator and the beams are made of aluminum nitride (AlN) which was chosen among other piezoelectric materials for its high acoustic velocity (10 927 m/s), a good piezoelectric coefficient (1.55 C/m^2) and a good thermal conductivity [21].

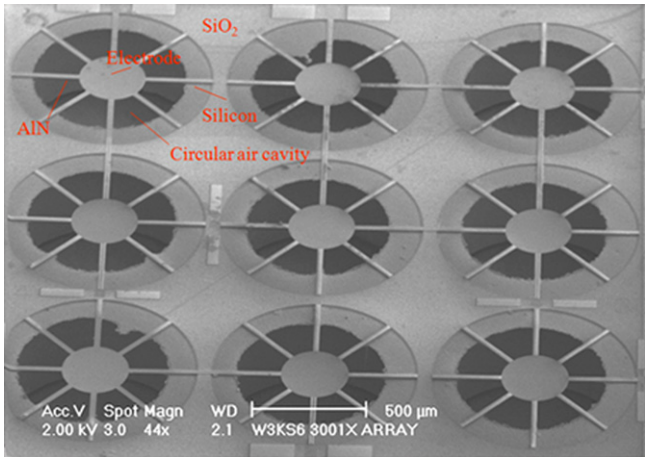

Fig. 1. The 3×3 array of aluminum nitride trampoline resonators fabricated at UCSB. The circular resonators are 300 μm in diameter and 1.7 μm thick supported by eight beams 300 μm long. The resonators are suspended over an air cavity and respond to through thickness vibrations.

The beams electrically connect the resonator via a MEMS component attached to the far ends. They are expected to minimize the transfer of acoustic energy from the resonating element to the surrounding system and diminish attachment loss that would result from clamping the membrane to the substrate. A gold electrode approximately 0.27 μm thick covers the top circular portion of the resonator so the beams are not piezoelectrically activated. The device is driven by a 1.5 GHz AC current oriented parallel to the axis of polarization in order to enable longitudinal (though-thickness) vibrations. The magnitude of the input current takes into account the electrode's added mass which has for effect to decrease the magnitude of the resonant frequency according to a simple one dimensional undamped spring-mass model.

Fabrication techniques specific to the UCSB design can be found in [24]. They include an Inductively Coupled Plasma (ICP) chlorine process to etch the AlN and a MEMS-based bulk silicon Deep Reactive Ion Etch (DRIE) process to form a circular air cavity. The AlN film is sputtered directly onto a $\langle 100 \rangle$ silicon wafer.

A resonator performance is characterized by means of the electromechanical coupling coefficient K^2 and the quality factor Q. K^2 combines the elastic, piezoelectric and dielectric material coefficients [25] and is defined as the ratio of electrical energy to mechanical energy stored in the device. A high value of K^2 is desired and associated with a broad bandwidth. The Q-factor measures mechanical losses due to internal or external sources and is an indication of the sharpness of the resonant response of the system. For filters, the parameters can be combined into the product K^2Q, which indicates lower insertion loss and better efficiency when high [23]. In theory, infinite values of Q can be achieved but in practice, values of Q on the order of only 10^3 are expected in this kind of electronic applications [1] because filters have complex geometries and energy can dissipate at many locations (i.e. electrodes, supporting and surrounding medium, anchor points). In terms of damping ratio ($\zeta = 1/2Q$), values in the order of 0.05% or smaller are typical for these applications.

Experimental values for the device fabricated at UCSB were obtained with a network analyzer. Performance values reported in [24], $K^2 = 6.3\%$ and $Q = 150$ at 1.5 GHz are significantly higher values than those reported in the literature for similar designs, $Q = 91.7$

and $K^2=2.4\%$ at 1.65 GHz and $Q=50.2$ and $K^2=1.2\%$ at 1.64 GHz for square-shape aluminum nitride resonators supported by beams, $160\times160\ \mu m^2$, 2 μm-thick and $200\times200\ \mu m^2$, 15 μm-thick, respectively [10]. However, the figures obtained are not yet in the order of the thousand expected for this kind of applications. To investigate possible causes for this low Q, we have engaged in a systematic parametric study of the resonators using Abaqus [26], a three-dimensional finite element commercial package. The primary quantities we estimate are the resonant and anti-resonant frequencies, the electromechanical coupling coefficient K^2 and the quality factor Q. We also identify spurious modes of resonance and their proximity to the important fundamental modes since the excitation of spurious modes results in energy loss and a degraded Q-factor. The other FEM modeling of piezoelectric resonators we are aware of are used to validate a particular design while ours is intended to serve in the design stages to eliminate the difficulties, length and high costs that would result in fabricating a poor performance device.

Among researchers who have used three-dimensional finite element models to develop and optimize piezoelectric resonators are Antkowiak et al. [9], who use finite element state-based modeling procedures to study (-very similarly to our work) the performance characteristics of AlN MEMS film bulk acoustic resonators 3 μm wide, 6 μm long and 0.5 μm thick, excited longitudinally. However, the input geometry is modeled with less than one hundred nodes and calculations are performed with Mathcad. Jung et al. [14] analyzed the resonance modes of a 1 μm thick zinc-oxide (ZnO) FBAR device in addition to the spurious modes of resonance caused by variations in electrodes and found an optimum ratio of length to thickness. Southin et al. [15] showed that extensional resonances of rod-like length nanostructures yielded significant higher values of the electromechanical coupling coefficient compared to the plate-like longitudinal resonance typical of FBAR geometry. In [16], Zhu et al. presented a new modeling approach combining microwave circuit theory and finite element analysis to study a mechanical filter comprised of two mechanically coupled silicon cantilevers and determined the optimum position and length of the linkage for maximum Q-factors. More recently, Yong et al. [17] have proposed a method to solve the equations of piezoelectricity including damping and losses due to current conduction without using usual a-priori assumptions for the resonator impedance or resistance and concluded that eigenvalues from free vibration analysis can be used for designing high-Q resonators.

The methodology we used to study the optimal design configuration for the filter consisted in breaking the analysis into four phases from a simplified to a more complex model, with the anticipation that the resonator that had achieved the best performance singly would result in a high performance filter as well. Fig. 2 shows the different levels of idealization. This paper reports the results of the first phase in which the resonators are subjected to systematic variations in thickness, number of beams and beam length. The beam width has not been studied. For a first level of approximation, we assumed that the electrodes were so thin that their mass-loading effect was negligible. The second phase consisted in using the resonator geometry that had shown optimized performance and to account for the effects of two electrodes (a top gold electrode and a bottom aluminum electrode). This differed slightly from the fabricated device which utilized one electrode at the time. The third phase considered the more complete model of the resonator with electrodes resting on a silicon substrate. The results of the second and third phase have been reported in [27]. The final phase arranged the resonators in pairs (1×2 array) and in quad (2×2 array) to model the filter and to study the nature of the interactions (i.e. cross talk or energetic coupling) from one resonator to another.

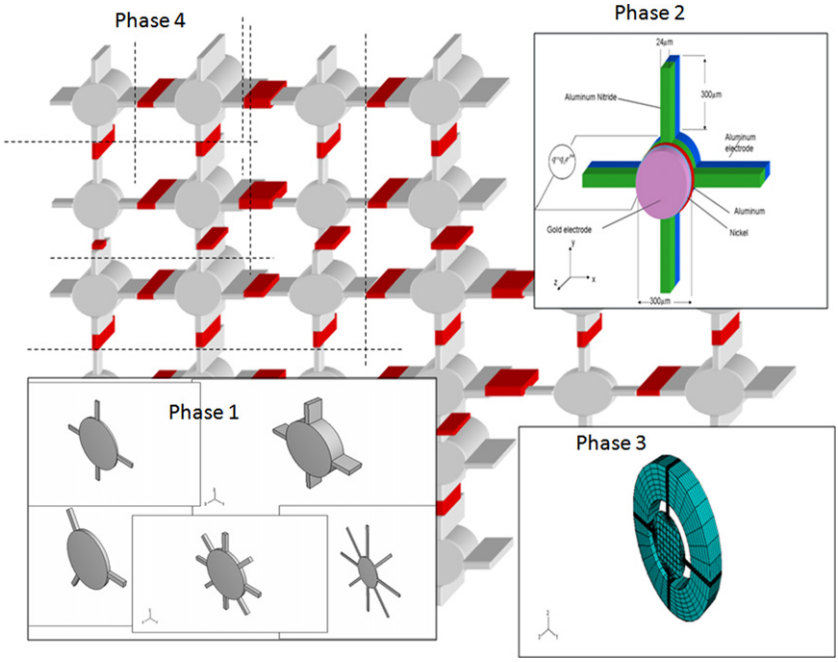

Fig. 2. Different levels of idealization used in the parametric study of the resonator.

Material damping has been accounted for in all the simulations as explained in the following section but we did not consider losses due to thermal dissipation of current in the structure. This is nonetheless an active area of research (see for instance [12,13–28]). Another concern reported in the manufacturing community has been to determine if there is a need to vacuum package MEMS devices as a way to limit energy loss due to air exposure [19,20]. Test data [24] indicated that neither viscous air damping nor damping arising from acoustic radiations were significant loss mechanisms.

2. Theory

Details pertaining to the analytical treatment of piezoelectric materials can be readily found in the literature [25]. The relevant equations are

$$\{T\} = [C^E]\{S\} - [e]^T\{E\},$$
$$\{D\} = [e]\{S\} + [\varepsilon^S]\{E\}, \quad (1)$$

provided constant temperature and lossless process are assumed and where in Cartesian coordinates, $\{\boldsymbol{T}\}^T = \{T_{11}\ T_{22}\ T_{33}\ T_{23}\ T_{13}\ T_{12}\}$ is the array of stress components, the superscript T indicating the transpose, $\{\boldsymbol{S}\}^T = \{S_{11}\ S_{22}\ S_{33}\ S_{23}\ S_{13}\ S_{12}\}$ is the array of strain components, $\{\boldsymbol{E}\}^T = \{E_1\ E_2\ E_3\}^T$ is the array of electric field components, and $\{\boldsymbol{D}\}^T = \{D_1\ D_2\ D_3\}^T$ is the array of components of electric displacements.

Piezoelectric materials undergo strains in the order of 0.1% so the small deformation theory can be assumed in which the strains are given in terms of the displacement gradients *as* $S_{ij} = (u_{i,j} + u_{j,i})/2$, where $u_{i,j}$ indicates the partial differentiation of the displacement u_i with

respect to position x_j. The components of electric field are given by the gradient of the electric potential φ, i.e. $E_{,i}=-\varphi_{,i}$ .The symbols $[\boldsymbol{c}^{\boldsymbol{E}}]$, $[\boldsymbol{\varepsilon}^{\boldsymbol{S}}]$ and $[\boldsymbol{e}]$ refer to the elasticity matrix at constant electric field, the dielectric permittivity matrix at constant strain and the matrix of piezoelectric coefficients, respectively. Strains and stresses can be calculated from the solution of the displacement field while the solution of the electrical potential yields the electrical impedance, a quantity defined as the ratio of voltage over the electrical current and from which performance figures can be calculated.

In the absence of body forces, conservation of linear momentum is assured by $T_{ij,j}=\rho u_{i,tt}$ where ρ is the material density and where the subscript t after a comma denotes partial differentiation with respect to time. Conservation of angular momentum is enforced by symmetry of the stress tensor. For the electrical part of the problem, the acoustic limit rather than the electromagnetic limit is imposed and conservation of electric flux in the absence of free charge is assured by Gauss's law in the form $D_{i,i}=0$ (i.e. the divergence of the electric displacement is zero), another form of the quasi-static assumption for the elastic fields.

These equations are augmented by prescribed mechanical and electrical boundary conditions on the surface A of the domain under consideration. For the surfaces of the resonator (excluding the electrodes) denoted by A_t with outward unit normal vector $\boldsymbol{n}$, the traction $t_i=T_{ij}n_j$ is prescribed. On the remaining portion of the surface (A_u), the displacement u_i is prescribed. For the surfaces representing the electrodes (A_φ), the electric potential is prescribed while the remainder of the surface (A_D) is charge-free so that the normal component of the electric displacement is zero (i.e. $n_iD_i=0$)

Virtual work for the body is expressed as

$$\int_{\mathrm{V}}\{\boldsymbol{\delta u}\}^T\rho\{\boldsymbol{u}\}_{,\boldsymbol{tt}}\,dV+\int_V\{\boldsymbol{\delta S}\}^T\{\boldsymbol{T}\}\,dV=\int_{A_T}\{\boldsymbol{\delta u}\}^T\{\boldsymbol{t}\}\,dS,$$

$$\int_V\{\boldsymbol{\delta E}\}^T\{\boldsymbol{D}\}\,dV=-\int_{A_D}\delta\varphi n_iD_i\,dS, \tag{2}$$

where the symbol δ indicates a virtual variation of the term immediately following it. When the piezoelectric relationships in (1) are used in conjunction with the standard interpolations of the finite element method, for a model having m nodes, the $4m$ coupled ordinary differential equations of the finite element method are obtained from virtual work [29] as

$$\begin{bmatrix}[\boldsymbol{M}] & \boldsymbol{0}\\ \boldsymbol{0} & \boldsymbol{0}\end{bmatrix}\{\boldsymbol{\Delta}\}_{,\boldsymbol{tt}}+\begin{bmatrix}[\boldsymbol{C}] & \boldsymbol{0}\\ \boldsymbol{0} & \boldsymbol{0}\end{bmatrix}\{\boldsymbol{\Delta}\}_{,\boldsymbol{t}}+\begin{bmatrix}[\boldsymbol{K}_{\boldsymbol{uu}}] & [\boldsymbol{K}_{\boldsymbol{u}\varphi}]\\ [\boldsymbol{K}_{\boldsymbol{u}\varphi}]^T & [\boldsymbol{K}_{\varphi\varphi}]\end{bmatrix}\{\boldsymbol{\Delta}\}=\{\boldsymbol{P}\}, \tag{3}$$

where the coefficient matrices in this system are square with size $4m\times 4m$. In (3), $\{\boldsymbol{\Delta}\}^T=\{\boldsymbol{u}_n\boldsymbol{\varphi}_n\}^T$ is an array containing in the first $3m$ locations, the nodal displacements u_n (where n stands for nodes) of the finite element model and followed in the next m locations by the electric potential values $\boldsymbol{\varphi}_n$ at the nodes of the model. Similarly $\{\boldsymbol{P}\}^T=\{\boldsymbol{F}_n\boldsymbol{Q}_n\}^T$ is an array containing in the first $3m$ locations, the applied nodal forces $\boldsymbol{F}_n$ and followed in the next m locations by the applied nodal charges $\boldsymbol{Q}_n$.

The applied nodal forces are statically equivalent to surface tractions and the applied nodal charges are electrostatically equivalent to surface charge densities [30]. The entries in (3) are the $3m\times 3m$ mass matrix $[\boldsymbol{M}]$, the $3m\times 3m$ damping matrix $[\boldsymbol{C}]$. Finally, $[\boldsymbol{K}_{\boldsymbol{uu}}]$ represent the $3m\times 3m$ stiffness matrix, $[\boldsymbol{K}_{\boldsymbol{u}\varphi}]$ is the $3m\times m$ piezoelectric coupling matrix and $[\boldsymbol{K}_{\varphi\varphi}]$ is the $m\times m$ capacitance matrix. The columns and rows of the relevant matrices

not filled by the mass and damping matrices are zero, as indicated in (3). All matrices and arrays in (3) are computed automatically by Abaqus and their detailed form in terms of finite element theory can be found in [29].

Note that damping which is absent in (1), has been introduced in the finite element solution to account for energy dissipated by all mechanisms other than material yielding. In our work, we used a particular form of damping known as Rayleigh damping where damping is written as a linear combination of the mass and stiffness matrices via two non-negative scalar coefficients α and β namely $[\boldsymbol{C}]=\alpha[\boldsymbol{M}]+\beta[\boldsymbol{K_{uu}}]$ [31]. This form has the advantage to yield a set of uncoupled orthogonal modal equations of motion and to significantly reduce the computing time. The steps used to quantify the coefficients α and β are discussed later.

3. Finite element methodology

The mechanical and electrical boundary conditions enforced in the simulations are shown in Fig. 3. All external surfaces are stress free ($\boldsymbol{T}=0$) except the ends of the beams which are fixed ($\boldsymbol{u}=0$). This condition is enforced based on the assumption that the substrate is massive and stiff compared to the resonator, so the ends of the beams where they are attached to the substrate are fixed in position. The surfaces for which no electrical potential is specified are charge free ($\boldsymbol{D}\cdot\boldsymbol{n}=0$) where $\boldsymbol{n}$ represent the normal vector to the surface. The bottom surface of the resonator has zero potential ($\varphi=0$) to represent a grounded electrode while the top surface is maintained at a uniform potential ($\varphi=\varphi_0$). Consequently, all the nodes on a given electrode experience the constraint that their electrical potential is tied to one value, eliminating the equations in (3) for the electric potential of all these nodes except one retained node on that electrode. Furthermore, the nodal electrical charges to the right hand side of (3) for these nodes are aggregated into one value representing the total charge on a given electrode. For the two electrodes these total charges are equal in magnitude and opposite in sign. Thus, the entire right hand side of (3) can be represented by one parameter, namely the total charge, Q_e on one of the electrodes,

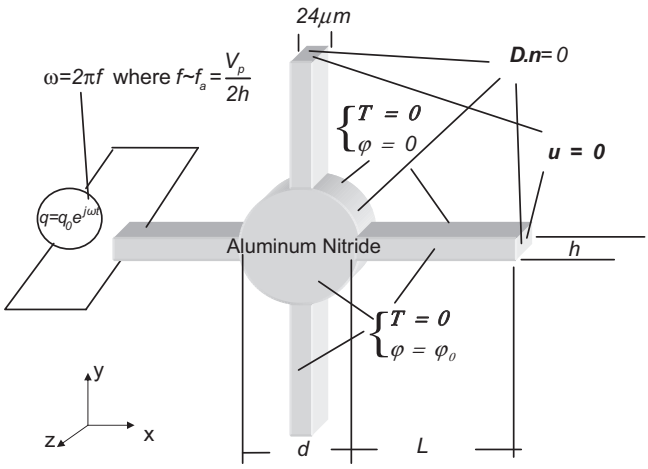

Fig. 3. Mechanical and electrical boundary conditions enforced in the simulations.

which has potential φ_e, with the other electrode held at zero potential and having total charge $-Q_e$. As a result, a simple strategy can be adopted for the solution of the frequency response of the FBAR, which is to drive the total charge on the electrodes at a frequency ω and amplitude q_0, so that $Q_e=q_o e^{j\omega t}$, with $j=\sqrt{-1}$, and to use (3) to compute the resulting amplitude and phase of the potential difference between the electrodes. The phase angle, $\psi(\omega)$, gives the degree to which the charge on the electrodes lags the potential difference between the electrodes due to damping. The result for the potential difference between the electrode is approximately $\varphi_e(\omega,\psi,t)=\varphi_o(\omega)e^{j(\omega t+\psi)}$, where φ_0 is the amplitude of potential difference between the electrodes. The approximation arises because, for the finite element model, (3) represents a multi-degree of freedom system and when driven at a specific frequency, the response will involve a multiplicity of modes each having its own amplitude and phase angle. Thus it should be understood that the concepts just described are meaningful strictly only when the frequency is very near one of the natural frequencies, and so the response of the FBAR system is dominated by the shape, amplitude and phase angle of the mode associated with that natural frequency.

The methodology in Abaqus involves a sweep of the driving frequency from a low value to a high value. The range of the driving frequency is confined to a limited interval that contains the expected fundamental natural frequency and obtained from the eigenvalue analysis returned by Abaqus. Within this range, (3) is solved repeatedly and an approximately sinusoidal curve in time for the potential difference is obtained from the output. The amplitude of the potential difference is obtained from the peak to peak magnitude and the phase angle is obtained by the degree to which the peak in the potential difference leads the peak of the total charge sine wave. Note that the eigenvalues (found from solving the homogeneous form of Eq. (3)) are computed without damping which result in an infinite number of values because the diagonal terms of the electrical degrees of freedom in the mass matrix are not zero. To find the associated finite eigenvalues (squares of the natural frequencies), we used a Lanczos method to diagonalize and orthogonalize the matrices. Details of the procedure are given by Guo et al. in [32] and can also be found in the Abaqus documentation [26].

4. Device performance

A resonator behavior is characterized by it electrical impedance $Z(\omega)$ defined for a single degree of freedom system as [25]

$$Z(\omega)=\frac{V(\omega)}{I(\omega)}, \tag{4}$$

where $I(\omega)$ is the electrical current at an electrode, i.e. the rate of change of total charge on the electrode and the voltage $V(\omega)$ is the potential difference between the electrodes. Written in polar form, $Z(\omega)=|Z(\omega)|e^{-j\zeta(\omega)}$, with the electrical impedance magnitude and phase angle given in terms of the parameters introduced in the previous paragraphs by $|Z(\omega)|=\varphi_0(\omega)/\omega q_0$ and $\zeta(\omega)=\pi/2-\psi(\omega)$.

Another form of the electrical impedance of a piezoelectric resonator undergoing longitudinal vibrations can be shown to be

$$Z(\omega)=\frac{1}{j\omega C_0}\left\{1-K^2\frac{\tan(k_p h/2)}{(k_p h/2)}\right\}, \tag{5}$$

where h is the piezoelectric slab thickness, k_p is the wave number defined as $k_p=\omega/V_p$, $V_p=\sqrt{(Y_p^D/\rho)}$ is the wave velocity in the piezoelectric material, Y_p^D is the piezoelectric material equivalent stiffness defined as $Y_p^D=C_{33}+e_{33}^2/\varepsilon_{33}$ (the subscript 3 representing properties in the thickness direction) , C_0 is the static device capacitance defined by $C_0=\varepsilon_{33}A/h$, where A is the planform area of the piezoelectric slab, and K^2 is given by $K^2=e_{33}^2/\varepsilon_{33}\ Y_p^D$ [25]. The form (5) uses a one-dimensional model and assumes that the material is free from damping. With the material properties for AlN given in Table 1, the wave velocity is $V_p=10927$ m/s and the effective acoustic coupling coefficient is $K^2=5.88\%$. This value differs from the one given in [24] ($K^2\sim6.5\%$) because of the material properties we used.

Resonance (or series resonance) occurs for each value of h that causes $Z(\omega)$ to be zero and anti-resonance (or parallel resonance) takes place when $Z(\omega)$ is equal to infinity. With that, the magnitude (real part) of the electrical impedance may be rearranged to approximate K^2 as a function of the relative separation between the resonant f_r and anti-resonant frequencies f_a of the system

$$K^2=\frac{\pi^2}{4}\left(\frac{f_a-f_r}{f_a}\right), \tag{6}$$

assuming that both frequencies are negligibly different compared to the magnitudes of the frequencies themselves [25].

The parameter Q measures energy loss due to internal or external sources and is evaluated from the phase angle (imaginary part) of the electrical impedance using the

Table 1
Materials properties.

	Aluminum nitride	Silicon
Density ρ (kg/m^3)	3512	2300
Elastic constants (GPa)	Orthotropic (transverse isotropy) $C_{11}=C_{22}=345$ $C_{12}=125$ $C_{13}=C_{23}=120$ $C_{33}=395$ $C_{44}=C_{55}=118$ $C_{66}=110$	Cubic isotropy $C_{11}=C_{22}=C_{33}=165.7$ $C_{12}=C_{13}=63.9$ $C_{44}=C_{55}=C_{66}=79.6$
Dielectric permittivities (10^{-12} Farad/m)	Orthotropic $\varepsilon_{11}=\varepsilon_{22}=79.65$ $\varepsilon_{33}=97.35$	Isotropic $\varepsilon_{11}=\varepsilon_{22}=\varepsilon_{33}=104.43$
Piezoelectric constants (Coulomb/m^2)	$e_{24}=e_{15}=-0.48$ $e_{31}=e_{32}=-0.58$ $e_{33}=1.55$	
Poisson's ratio		0.22
Wave velocity (m/s)	10,927	
Elastic impedance (10^6 kg/m^2/s)	38	
Material damping β (10^{-14} s)	2.82	3.2

relation

$$Q_{r,a} = \frac{f_{r,a}}{2}\left|\frac{d\zeta}{df}\right|_{f_{r,a}}, \tag{7}$$

where $\left|d\zeta/df\right|_{fr,fa}$ is the absolute value of the derivative of the phase ζ with respect to the resonant or anti-resonant frequency [22].

A small difference between the two values Q_r and Q_a is an indication that the system is lightly damped. Strictly speaking, the values of the resonant and anti-resonant frequencies used in determining K^2 differ from those used in calculating Q. However, the values of the resonant and anti-resonant frequencies are not greatly affected by a light damping so the natural frequencies obtained from a basic eigenvalue analysis can be used.

5. Evaluation of Rayleigh damping coefficients

As mentioned above, damping in a system cannot in general be represented by a matrix satisfying the eigenvector orthogonality equation but Rayleigh damping employs a particular form of damping which results in a set of uncoupled orthogonal modal equations of motion [31]. The system Q-factors is then given as [26]

$$1/Q_r = \alpha/\omega_r + \beta\omega_r, \tag{8}$$

where ω_r is the particular frequency of vibration. This shows that mass proportional damping (given by the α coefficient) is used to damp out the lowest frequency response and stiffness proportional damping (given by the β coefficient) is used to damp out the highest frequency response. Physically, the α coefficient simulates the process of a model moving through a viscous medium so that any motion of any point in the model causes damping while the β coefficient can be thought as internal damping associated with the material itself [26]. To account for damping and to enter numerical values for the α and β coefficients in the simulations, we proceeded to an eigenvalue (unforced, undamped) analysis. It showed that resonance occurred around the 140th mode so that the lower frequency modes did not greatly contribute to damping and α was assumed to be zero throughout the work. The β coefficient is characteristic of the acoustic wave propagation which in a piezoelectric material requires the knowledge of the material stiffness, piezoelectric and dielectric constants and attenuation data. Compared to other piezoelectric materials such as ZnO [7] or PZT [18] used in similar applications, material properties of AlN are still scarce. Consequently, we assumed that values of attenuation in AlN were comparable to those of silicon. The reasoning was that the device was resting on a silicon substrate and similar damping behaviors in the two materials were needed to insure continuity of wave attenuation. In addition, AlN has a coefficient of thermal expansion comparable to that of silicon that insures continuity of stress due to temperature gradient. We proceeded to solve the one-dimensional viscoelastic wave equation using the material properties of silicon

$$c_0^2(\partial^2 w/\partial z^2) + \mu/\rho(\partial^3 w/\partial t\partial z^2) = (\partial^2 w/\partial t^2), \tag{9}$$

where $c_0 = \sqrt{(Y/\rho)}$ is the wave speed in the undamped material, Y is the material elastic stiffness (C_{33}), μ is the material viscosity in a Maxwell model for viscoelastic response, so that the viscous stress is $\mu(\partial^2 w/\partial t\partial z)$ where w is the particle displacement in the z-direction. The ratio μ/Y has the unit of time and consequently, it can be evaluated from the results of attenuation and velocity measurements.

Solutions of (9) can be written in the form $w(z,t)=Ae^{\pm(\lambda_1+j\lambda_2)z+j\omega t}$ where A is a constant and

$$\lambda_{1,2}=\frac{\omega}{c_0\sqrt{2}}\frac{1}{\sqrt{1+(\mu\omega/Y)^2}}\sqrt{\sqrt{1+\left(\frac{\mu\omega}{Y}\right)^2}\mp 1}. \tag{10}$$

These solutions are waves traveling and decaying in the negative and positive z directions, determined by the upper and lower signs respectively. The imaginary part λ_2 is associated with the velocity at which the wave propagates (ω/λ_2) while the real part λ_1 referred as the attenuation coefficient characterizes the damping and is a measure of the decrease in amplitude of the wave with distance.

For frequencies in the UHF range ($f\geq 1$ GHz), the ratio ($\mu\omega/Y$) is small compared to unity and approximations show that the wave speed drops from $\sqrt{(Y/\rho)}$ to $\sqrt{(2\mu\omega/\rho)}$. In the same manner, the coefficient λ_1 can be approximated as $\lambda_1\approx(\omega^2\mu\sqrt{\rho})2Y^{3/2}$ yielding the approximate value of the damping coefficient β in terms of material constants as $\beta=\mu/Y\approx(2\lambda_1/\omega^2)\sqrt{(Y/\rho)}$. Values of attenuation coefficients are commonly given in units of dB/m and can be expressed in the form of attenuation per unit travel-distance of the propagating wave. From the attenuation data in silicon (6.5 dB/cm at $f\sim 1$ GHz [33]), the value of λ_1 was calculated to be $\lambda_1=74.8\ \mathrm{m}^{-1}$ and substitution of the material constants of silicon (Table 1) into the relevant expression yielded $\beta=2.82\times10^{-14}$ s. This is the value used in the finite element simulations to account for material damping in AlN. Later on, Ref. [34] in which a value of damping in AlN is reported ($\beta=3.2\times10^{-14}$ s) came to our attention. The difference between the two values is due to the fact that we initially used a Poisson's ratio $v=0.28$ yielding $C_{33}=130$ GPa whereas using $v=0.22$ would have yielded $C_{33}=165.7$ GPa and $\beta=3.2\times10^{-14}$ s. Note that using $\beta=2.82\times10^{-14}$ s and $\omega_a=(2\pi)$x $3.17.10^9$ rad/sec in ($1/Q=\alpha/\omega_a+\beta\omega_a$) yields $Q=1780$, a value very close to the one retuned from the simulations as we will see next. Also note that using $\beta=3.2\times10^{-14}$ s with the same value of ω_a would yield $Q=1598$, a value close enough to the previous to warrant that simulations need not be redone.

6. Simulation results

The material properties used in the simulations are summarized in Table 1. All simulations use an eight-node, three dimensional piezoelectric brick element (C3D8E) with four degrees of freedom per node, corresponding to three components of displacement and one component of electrical potential. Careful evaluation of meshes has shown that the gain in accuracy was minimal with mesh refinement so a somewhat coarse mesh was used throughout the work.

For each simulation, we generated the electrical impedance frequency response and calculated the performance figures K^2 and Q. Each simulation has set of indices that refer to the resonator's geometry and dimensions, namely: diameter, number of beams, beams length and thickness. For instance, d300-4l-100-1.7 is a resonator 300 μm in diameter with four beams 100 μm long and 1.7 μm thick. The beam widths are all 24 μm wide. The beams and the resonator have the same thickness.

Fig. 4 is an illustration of the electrical impedance frequency response generated from the simulations of the d300-4l-100-1.7 resonator. The sharp pick at 3.17 GHz indicates the value of the frequency at which (anti)-resonance takes place and where the resonator is clearly strained in the thickness direction as evidenced by the picture. A simple one dimensional

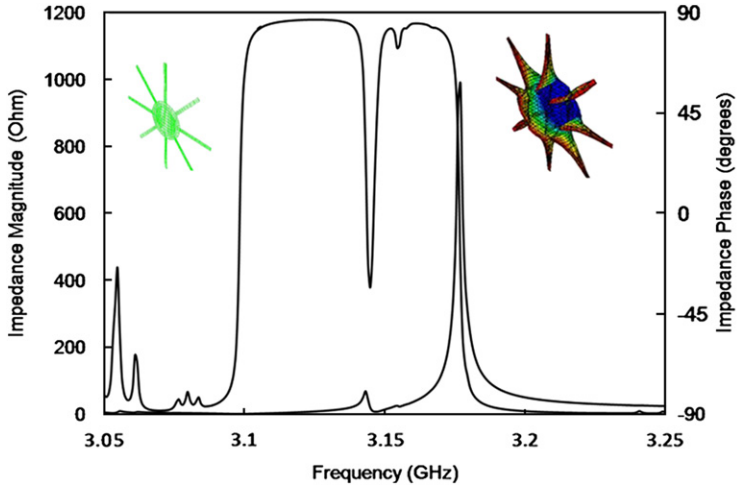

Fig. 4. Electrical impedance frequency response of the resonator (d300-8l-300-1.7). The sharp pick at 3.17 GHz indicates the (anti)-resonance frequency at which the resonator is clearly strained in the thickness direction. Also shown is the resonator at rest.

analysis gives a value of 3.21 GHz and compares well with the simulation value. The small discrepancy is due to the fact that the simulations are three-dimensional and include damping. As expected, the damped system (simulated) resonates at a frequency lower than the one that would result in an undamped system.

6.1. Resonator thickness

The effect of the resonator thickness on the magnitude of the (anti)-resonant frequency is illustrated in Fig. 5. It shows the decaying variation of the (anti)-resonant frequency with the material thickness. The simulations obtained for four-beam resonators (d300-4l-100) confirmed that for a lightly damped system, anti-resonant frequencies values are very close to the one dimensional undamped system. It also shows that theoretically, frequencies above the 3 GHz range can be attained using AlN as the piezoelectric material. However, this would be difficult to reach in practice because there is a limit to how thin the device can be.

Plotted in Fig. 6 are the performance coefficients K^2 and Q obtained as a function of the resonator thickness. K^2 remains almost unaffected by the resonator thickness topping at about 6.15%, a value very close to the one obtained with the one dimensional undamped model calculated with the equation $K^2=e_{33}^2/(\varepsilon_{33}C_{33}+e_{33}^2)$ [25] (the subscript 3 representing material properties of AlN in the thickness direction) and yielding $K^2=6.24\%$ in excellent agreement with the one measured experimentally (6.3% [24]). (Note that [21] reports $K^2\sim6.5\%$ but uses slightly different material properties). Q's obtained from the simulations range from 997 to 4475 and increase linearly with the thickness. Furthermore, the expression $Q_a=h/(\beta\pi V_p)$ is readily obtained by substituting the one dimensional model for the first resonant frequency ($f_a=V_p/2h$) into the expression $Q_a=1/(\beta\omega_a)$ assuming $\alpha=0$ making it clear that Q_a values are proportional to the resonator thickness. Thus, thick resonators are capable of achieving high Q's but at the same time they resonate at a lower value which illustrates some of the design trade-off.

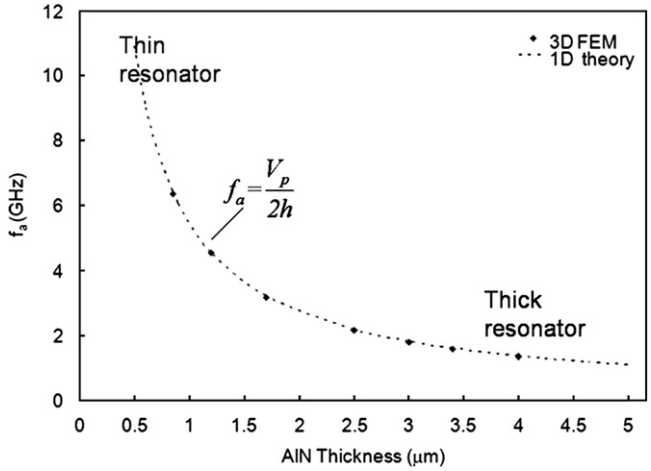

Fig. 5. Anti-resonant frequencies as a function of the resonator's thickness. The simulations are performed on resonators d300-4l-100-**. The results of the simulations agree well with those predicted by a one-dimensional theory.

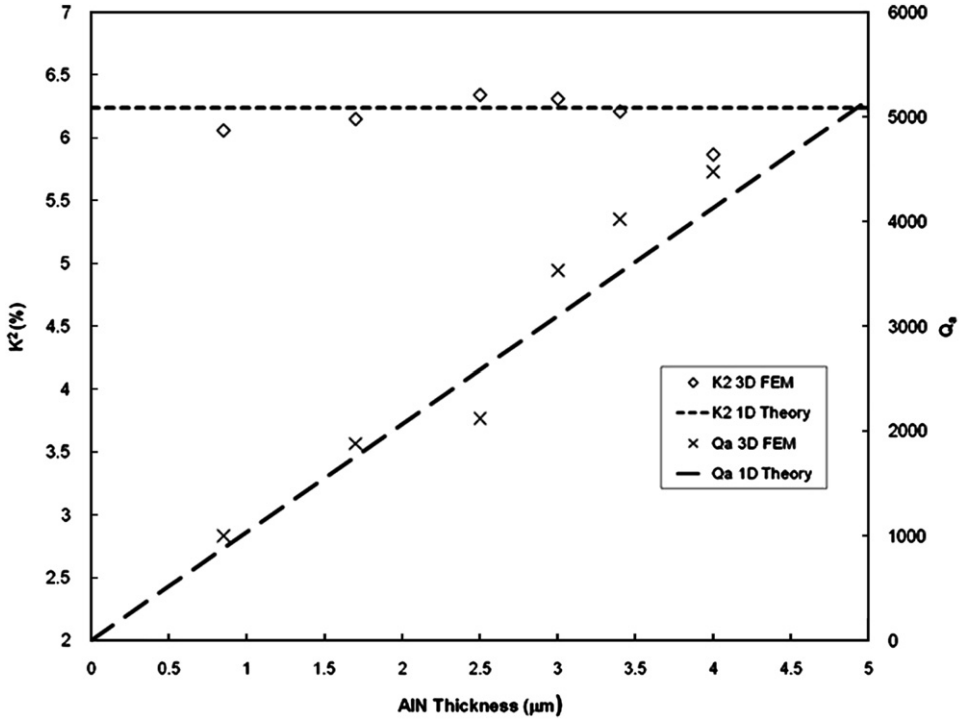

Fig. 6. Electromechanical coupling coefficient K^2 and Q-factor as a function of the resonator's thickness. The simulations are performed on d300-4l-100-** resonators. The results of the simulations agree well with those predicted by a one-dimensional theory. The theoretical one dimensional value $K^2 = 6.24\%$ is obtained with material's properties.

6.2. Beam length

Fig. 7 represents the variations of the electrical impedance frequency response for a resonator with eight beams (d300-8l-**-1.7) with the beam length. It clearly shows the presence of spurious modes between the resonant and anti-resonant frequency that become stronger with longer beams and also shifts to the right. On the other hand, the results suggest by extrapolation that if the beams are too short, the spurious modes would be in the proximity of the resonant frequency and would result in greater dissipation during resonance and a degraded Q_r.

Table 2 shows that resonators with shorter beams have a slightly higher value of K^2 (6.15%) but an almost constant Q factor ($Q\sim1750$). (The value of Q dropping to 1650 for 200 μm beam length seems to be an artifact of the simulations.) During the resonant phase, most of the energy is dissipated in the central portion of the resonator so the beam length

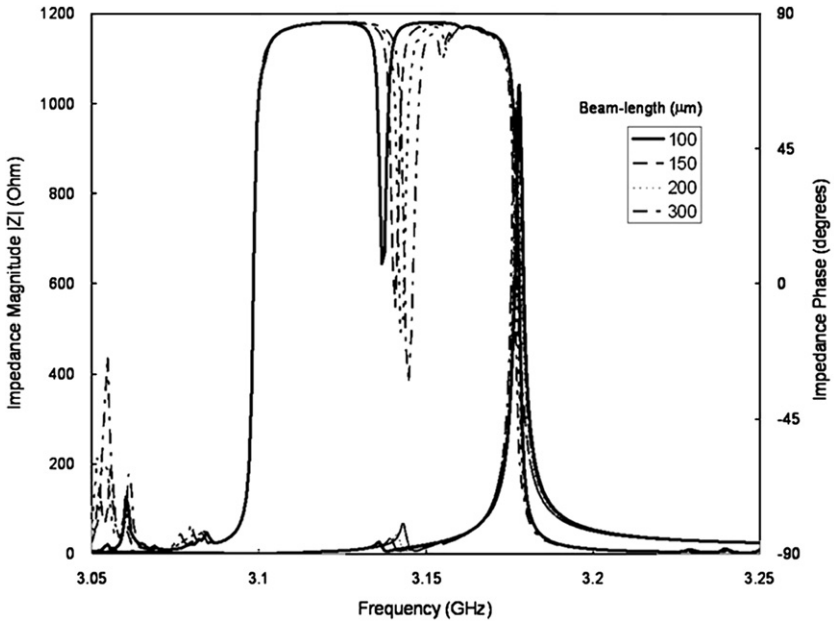

Fig. 7. Effect of beam-length on the electrical impedance frequency response. The spurious modes become stronger as the beam length is increased. The simulations are performed on resonators d300-8l-**-1.7.

Table 2
Effect of beam length on the performance coeffecients.

Beam length (μm)	K^2 (%)	Q	K^2Q
100	**6.15**	**1789**	**110.0**
150	**6.15**	**1730**	**106.4**
200	**6.09**	**1650**	**100.4**
300	**6.09**	**1786**	**108.7**

has minimal effect. Resonators with other beam lengths have also been fabricated at UCSB and test data [24] confirm the above result.

6.3. Number of beams

Fig. 8 shows how the number of beams affects the electrical impedance frequency response of d300-**-100-1.7 resonators. The interesting feature is that the resonator with three beams experiences resonance at 3.21 GHz or about 20 MHz higher than the resonator with four or eight beams, so we would expect a lower Q as explained above. However, the three-beam device has the highest Q (~1950) of all as seen in Table 3. Even though the eight-beam resonator has a slightly higher K^2, the combined product is higher for the three-beam resonator (K^2Q~118.7) and resonates at a higher frequency which makes it a better candidate in terms of performance. An explanation is that the three beams are approximately aligned with the three principal crystallographic directions of AlN (120^0 apart each), where material properties are identical and damping is minimal.

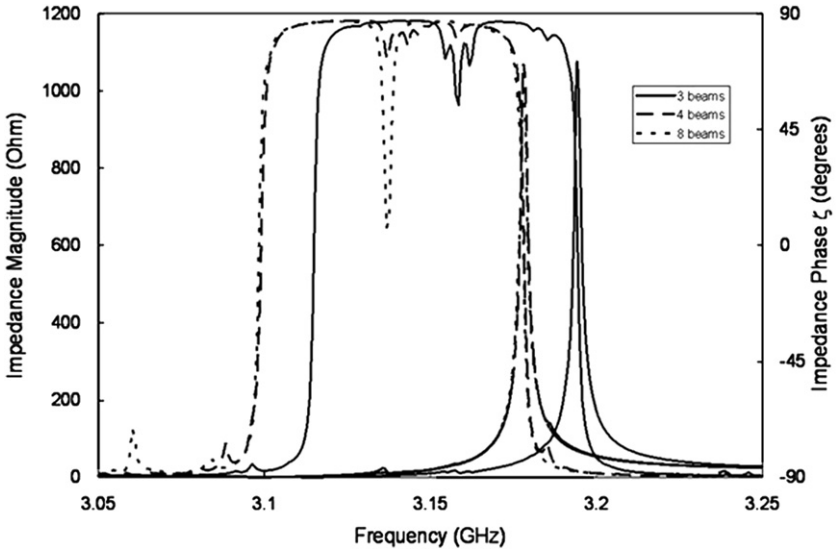

Fig. 8. Effect of number of beams on the electrical impedance frequency response. The three-beam resonator experiences (anti-) resonance at a higher frequency value than the resonator with four or eight beams. The simulations are performed on resonators d300-**-100-1.7.

Table 3
Effect of number of beams on the performance coefficients.

Number of beams	K^2 (%)	Q	K^2Q
3	**6.09**	**1950**	**118.7**
4	**6.09**	**1880**	**114.5**
8	**6.15**	**1789**	**110.0**

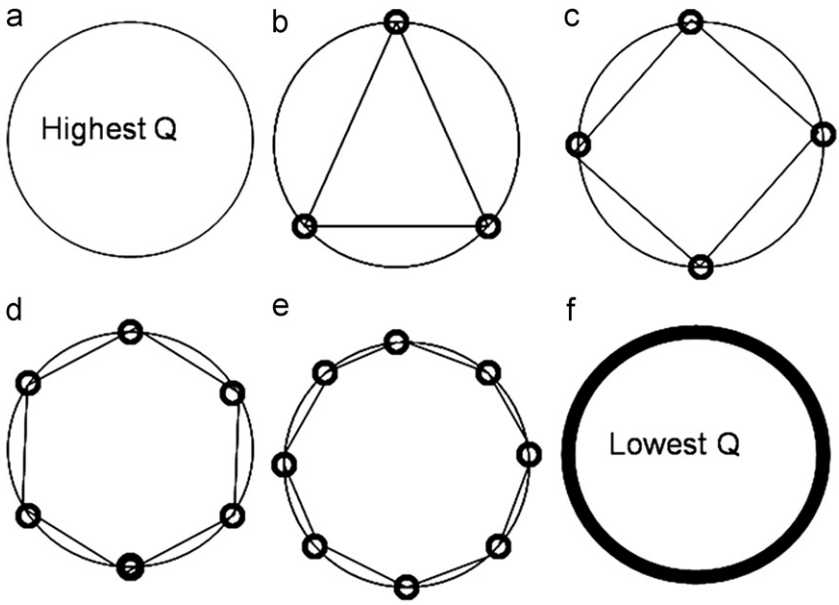

Fig. 9. Free–free and clamped circular resonator with intermediate cases. The three-beam case applies the least constraint to the resonator while the eight-beam applies the most. The beam-points of attachment to the circular resonator – not the beams themselves – are shown in the figure. (a) free-free, (b) 3 beams, (c) 4 beams, (d) 6 beams, (e) 8 beams, and (f) clamped.

Fewer beams apply less constraint or disturbance to the vibration modes of the center of the resonator and tend to eliminate rotational and/or radial components of the displacement. This is illustrated in Fig. 9. The resonant mode becomes closer to the ideal pure longitudinal mode where the circular portion of the resonator expands only in the thickness direction and for which Q is the highest. We note that this result contradicts test data which have pointed to a higher performance for the eight-beam resonator [24].

6.4. Damping coefficient

Our simulations have yielded $Q\sim1900$ for a 1.7 μm thick resonator, a value in good agreement with the one predicted by a one-dimensional theory ($Q\sim1756$) in which anti-resonance is dominated by the behavior of one frequency isolated mode. However, this is about ten times higher than the value measured for the device fabricated at UCSB [24] suggesting that damping modeling be revised altogether.

The most obvious difference between the model used in the simulations and the actual device is that electrodes have been neglected in the analysis. A subsequent model of the resonator with electrodes has been implemented [26] and simulations have retuned values of Q on the order of 1100. A silicon substrate has also been added in the model and has shown minimal additional effect with simulations results yielding $Q\sim1000$ [27]. Another reason for the discrepancy may be in the enforced condition that the ends of the beams are fixed in position (see Fig. 3) preventing energy dissipation into the substrate. This condition is too strong and should be relaxed. The UCSB team [24] has advanced that electrodes and silicon surface roughness as well as the electrical resistance of the transmission line were primarily responsible

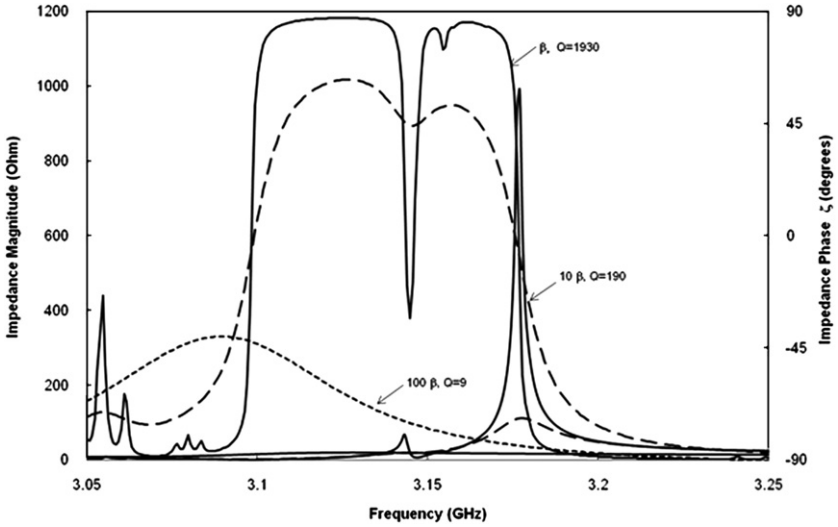

Fig. 10. Effect of damping coefficient β on the electrical impedance frequency response. The spurious modes are masked when the damping coefficient is increased. The simulations are performed on resonators d300-8l-300-1.7 using $\beta = 2.82 \times 10^{-14}$ s.

for degrading the Q-factors. Propagation of surface wave in the resonator may also result in energy loss [22]. This has not been modeled explicitly in our simulations but is not precluded.

This raises the possibility that the Rayleigh damping coefficient used in the simulations ($\beta = 2.82 \times 10^{-14}$ s) did not represent reality. Fig. 10 shows the electrical impedance frequency response for resonators d300-8l-300-1.7, when β is increased by ten and one hundred folds. As β is increased, the anti-resonance peak becomes less sharp as expected. Increasing β by a factor of ten decreases Q by a factor of ten, from $Q \sim 1900$ to $Q \sim 190$, a result expected from the elementary model ($Q_a = h/\pi V_p \beta$). In such case, the damping ratio ζ is 0.5%, a value still acceptable for a lightly damped system. However, increasing β one hundred times yields $Q \sim 9$ while the elementary model predicts a value about twice as much. The damping causes negligible change to the anti-resonance frequency so the discrepancy is not from that source. Instead, the inability of the elementary model to predict the Q-factor is probably due to interference among different modes, so that the assumption that Q can be estimated based on the response within one mode no longer holds. The fact that the spurious modes, visible for the lowest damping coefficient between the resonant and anti-resonant frequencies, are masked by the response with the largest damping coefficient is a clue that it is modal interference that is causing the discrepancy. The electromechanical coupling coefficient is almost constant $K^2 \sim 6.0\%$ for the three cases showing that the damping coefficient β does not greatly affect the value of K^2.

7. Summary

An optimal design configuration for an aluminum nitride MEMS resonator in the shape of a trampoline and designed for UHF filtering applications was investigated using three-dimensional finite element simulations. Performance was evaluated by means of the electromechanical coupling coefficient K^2 and the quality Q-factor which were calculated

from the magnitude and phase of the electrical impedance frequency response plots. The electrodes were assumed of negligible thickness so the magnitude of the resonant frequency was not affected by mass-loading effect. Material damping was accounted for in the simulations. Each resonator was forced by a harmonically varying electrical current oriented in the thickness direction over a range of frequencies containing the resonator's first natural frequency so that longitudinal resonant conditions could be observed.

The results indicated that (i) K^2 was insensitive to geometry ($K^2 \sim 6.5\%$), (ii) Q increased linearly with the AlN thickness attaining $Q \sim 1900$ for a 1.7 μm thick resonator and (iii) a trampoline resonator with three beams had a better performance capability than the resonator with four or eight beams with a figure of merit reaching $K^2Q \sim 120$ and resonating at a higher frequency value (3.21 GHz) than its counterpart resonators.

The trends and results compared well with those obtained from a one dimensional theory suggesting that key performance parameters could be evaluated from a simple one dimensional analysis. The main concern remained the discrepancy between the simulated and measured values of Q reported in [24] to being about ten times lower. However, electrodes which are well known mechanisms for energy dissipation were neglected in the analysis. This justified the need for a second-phase investigation in which the effects of electrodes were accounted for. Future work may also include a damping model other than Rayleigh damping which may not the best candidate to characterize the level of anisotropy of piezoelectric materials. Finally, losses due to thermal dissipation of the current should also be investigated.

Acknowledgments

This work was supported in part by the Defense Advanced Research Project Agency ONR/MINT under Contract N66001-01-1 8965. Fig. 1 was reproduced with permission of N.C. Mac Donald et al. at UCSB.

References

[1] C.T.–C. Nguyen, Microelectromechanical devices for wireless communications, in: Proceedings of the IEEE International Microelectromechanical Systems Workshop, Heidelberg, Germany, January 25–29, 1998, pp. 1–7.

[2] F.D. Bannon, J.R. Clark III, C.T.-C. Nguyen, High-Q high frequency micromechanical filters, IEEE Journal of Solid-State Circuits 35 (2000) 512–526.

[3] K. Wang, A.-C. Wong, C.T.-C. Nguyen, VHF free–free beam high-Q micromechanical resonators, Journal of Microelectromechanical Systems 9 (2000) 347–360.

[4] H. Kim, J.H. Kim, H.D. Park, G. Yoon, AlN-based film bulk acoustic resonator devices with W/SiO_2 multilayers reflectors for rf bandpass filter application, Journal of Vacuum Science & Technology B 19 (2001) 1164–1168.

[5] R.C. Ruby, P. Bradley, Y. Oshmyansky, A. Chien, J.D. Larson III., Thin film bulk wave acoustic resonators (FBAR) for wireless applications, in: Proceedings of the IEEE Ultrasonics Symposium, Piscataway, NJ, 2001, pp. 813–822.

[6] K.M. Lakin, Thin Film Resonators and High Frequency Filters, TFR Technologies, Inc., 2001.

[7] H. Zhang, E.S. Kim, Air-backed Al/Zno/Al film bulk acoustic resonator without any support layer, in: Proceedings of the IEEE International Frequency Control Symposium and PDA Exhibition, 2002, pp. 20–26.

[8] G.G. Fattinger, J. Kaitila, R. Aigner, W. Nesler, Thin film bulk acoustic wave devices for applications at 5.2 GHz, IEEE Ultrasonics Symposium (2003) 174–177.

[9] B. Antkowiak, J.P. Gorman, M. Varghese, D.J.D. Carter, A.E. Duwel, Design of high-Q low-impedance, GHZ-range piezoelectric MEMS resonator, in: Proceedings of the 12th International Conference Solid State Sensors, Actuators and Microsystems, Boston, June 8–12 2003.
[10] H.H. Kim, B.K. Ju, Y.H. Lee, S.H. Lee, J.K. Lee, S.W. Kim, Fabrication of suspended thin film resonator for application of RF bandpass filter, Microelectronics Reliability 44 (2004) 237–243.
[11] J.R. Clark, W. Hsu, A. Abdelmoneum, C.T.-C. Nguyen, U.H.F. High-Q, micromechanical radial-contour mode disk resonators, Journal of Microelectromechanical Systems 14 (2005) 1298–1310.
[12] A. Duwel, R.N. Candler, T.W. Kenny, M. Varghese, Engineering MEMS resonators with low thermoelastic damping, Journal of Microelectromechanical Systems 15 (2006) 1437–1445.
[13] R.N. Candler, A. Duwel, M. Varghese, S. Chandorkar, M. Hopcroft, W.T. Park, B. Kim, G. Yama, A. Partridge, M. Lutz, T.W. Kenny, Impact of geometry on thermoelastic dissipation in micromechanical resonant beams, Journal of Microelectromechanical Systems 15 (2006) 927–934.
[14] J.H. Jung, Y. Hyun Lee, Y. Hee Lee, H.C. Choi, Vibration-mode analysis of an RF film-bulk-wave resonator by using the finite element method, Journal of the Korean Physical Society 43 (5) (2003) 648–650.
[15] J.E. Southin, R.W. Whatmore, Finite element modeling of nanostructures piezoelectric resonators (NAPIERs), IEEE Transactions on Ultrasonics, Ferroelectrics, and Frequency Control 51 (6) (2004) 654–662.
[16] M. Zhu, P.B. Kirby, Design study of piezoelectric micro-machined mechanically coupled cantilever filters using a combined finite element and micro-circuit analysis, Sensors and Actuators A: Physical 126 (2) (2006) 417–424.
[17] Y.Y. Yong, M.S. Patel, Piezoelectric resonators with mechanical damping and resistance in current conduction, Science in China Series G: Physics, Mechanics and Astronomy 50 (5) (2007) 650–672.
[18] J.D. Larson III, S.R. Gilbert, B. Xu, PZT material properties at UHF and microwave frequencies derived from FBAR measurements, IEEE Ultrasonics Symposium 1 (August) (2004) 173–177.
[19] C. Zhang, G. Xu, Q. Jiang, Analysis of the air damping effect on a micromachined beam resonator, Mathematics and Mechanics of Solids 8 (2003) 315–325.
[20] Y. Yap, L.-K. Yap, W. Ye, Air damping in an ultra high frequency disk resonator, in: Proceedings of the Nanotech 2003, vol. 1 (11), pp. 316–319.
[21] A.N. Cleland, M. Pophristic, I. Ferguson, Single-crystal aluminum nitride nanomechanical resonators, Applied Physics Letters 79 (2001) 2070–2072.
[22] B.A. Auld, Acoustic Fields and Waves in Solids, Krieger, Malabar, FL, vol. I, 2nd ed., 1990 (Chapter 8).
[23] F. Rosenbaum, Bulk Acoustic Wave Theory and Devices, Artech House, Boston, 1988 (Chapters 4, 5, 10).
[24] L.A. Callaghan, V. Lughi, N.C. MacDonald, D.R. Clarke, Beam-supported AlN thin film bulk acoustic resonators, IEEE Transactions on Ultrasonics, Ferroelectrics, and Frequency Control 53 (2006) 1101–1107.
[25] E. Dieulesaint, D. Royer, Elastic Waves in Solids, John Wiley & Sons, 1980 (Chapter 7).
[26] Abaqus (now Simulia) Explicit/User's Manual, Version 6.4, Hibbitt, Karlson & Sorensen, Inc., 2003.
[27] A. Ruimi, Y. Liang, R.M. McMeeking, UHF aluminum nitride FBAR trampoline-shape resonators with gold-aluminum electrodes and silicon substrate with through thickness vibrations: computational performance, International Journal of Mathematics and Computation 1 (2008) N08.
[28] A.S. Vahdat, G. Rezazadeh, Effects of axial and residual stresses on thermoelastic damping in capacitive micro-beam resonators, Journal of the Franklin Institute 348 (4) (2011) 622–639.
[29] H. Allik, T.J.R. Hughes, Finite element method for piezoelectric vibration, International Journal for Numerical Methods in Engineering 2 (1970) 151–157.
[30] R. Lerch, Simulation of piezoelectric devices by two- and three-dimensional finite elements, IEEE Transactions on Ultrasonics, Ferroelectrics, and Frequency Control 37 (1990) 233–247.
[31] R.R. Craigs Jr., Structural Dynamics, An Introduction to Computer Methods, Wiley, 1981 (Chapter 18).
[32] N. Guo, P. Cawley, D. Hitchings, The finite element analysis of the vibration characteristics of piezoelectric discs, Journal of Sound and Vibration 159 (1999) 115–138.
[33] M.T. Wauk, Attenuation in Microwave Acoustic Transducers and Resonators, Ph.D. Dissertation, Stanford University, Stanford, CA, 1969.
[34] A. Ballato, J.G. Gualtieri, Advances in high-Q piezoelectric resonator materials and devices, IEEE Transactions on Ultrasonics, Ferroelectrics, and Frequency Control 41 (1994) 834–844.